Differential charge radii: Proton-neutron interaction effects

U. C. Perera ● and A. V. Afanasjev ●

Department of Physics and Astronomy, Mississippi State University, Mississippi 39762, USA

The analysis of self-consistency and proton-neutron interaction effects in the buildup of differential charge radii were carried out in covariant density functional theoretical calculations without pairing interaction on the example of selected configurations in the Pb isotopes. The proton-neutron interaction of neutron(s) added to the neutron $N = 126$ core and the protons forming the $Z = 82$ proton core is responsible for a major contribution to the buildup of differential charge radii. It depends on the products of proton and neutron wave functions and thus on their nodal structure. This interaction leads to a redistribution of single-particle density of occupied proton states which in turn modifies the charge radii. The microscopic origin of this redistribution and its consequences for differential charge radii were investigated for the first time. Self-consistency effects affecting the shape of proton potential, total proton densities and the energies of the single-particle proton states provide only minor contribution to differential charge radii.

I. INTRODUCTION

Charge radii are among the most fundamental properties of atomic nuclei, and during the last decade there was a significant increase in experimental and theoretical studies of this physical observable. The experimental results were reviewed in Refs. [1,2] and recent experimental investigations were summarized in the introduction of Ref. [3]. The introduction to the latter publication provides also the overview of theoretical efforts. Theoretical calculations within different density functional theories (DFTs) provide a quite accurate global description of experimental charge radii presented in the compilation of Ref. [1]: the rms deviations of calculated charge radii r_{ch} from experimental ones are at the level of ≈ 0.03 fm [4], which corresponds to high average precision of 0.625% in the prediction of charge radii (see Ref. [3]).

The changes of the charge radii within the isotopic chain are measured with high precision using laser spectroscopy (see Refs. [1,2]). Thus, the differential mean-square (ms) charge radii [see Eq. (3) below for definition], measured with high precision within the isotopic chains, become an important quantity. They have been studied within *ab initio* approaches (see, for example, Refs. [5,6]), nonrelativistic DFTs based on zero range Skyrme forces (see Refs. [7–10]), Fayans functional (see Refs. [11–13]) and finite range Gogny forces (see Refs. [5,14]), the nonrelativistic Hartree-Fock-Bogoliubov (HFB) approach with a finite-range Yukawa interaction [15–17], and covariant density functional theory (CDFT) (see Refs. [3,10,18–20]).

It is necessary to recognize that the microscopic mechanisms of the changes of charge radii with increasing neutron number or modification of the neutron configuration are not completely understood. This is because the absolute majority of the publications on the subject including those cited above deal only with total charge radii or their differences. The first hint on the microscopic origin of such changes was

provided in Ref. [21]: the difference of the charge radii on the occupation of the $2g_{9/2}$ and $1i_{11/2}$ neutron subshells in the $N > 126$ Pb isotopes is traced back to the nodal structure of these two subshells ($n = 1$ for $1i_{11/2}$ and $n = 2$ for $2g_{9/2}$, where n stands for principal quantum number). Note that the kink in differential charge radii at $N = 126$ is generated only when neutron $1i_{11/2}$ orbitals are substantially occupied in nuclei with $N > 126$ (see, for example, Refs. [3,8,21]). These results were generalized to the whole nuclear chart in Ref. [3] (see discussion of Fig. 32 in that reference): in a given isotopic chain the largest impact on differential charge radii above neutron shell closure is provided by the occupation of the neutron subshell with $n = 1$.

It is necessary to recognize that the studies of Refs. [3,21] leave many unanswered questions. For example, is the pull of neutron states on proton orbitals driven via the symmetry energy (as advocated in Ref. [21]) or it is due to proton-neutron interaction (as advocated in the present paper)? How are the modifications of the proton single-particle density distributions leading to changes in single-proton radii affected by the occupation of specific neutron states? What mechanism is responsible for this process? What role does the relative properties of the proton and neutron single-particle wave functions play in this mechanism? Thus, the goal of the present paper is to fill these gaps in our knowledge and to perform detailed studies of the impact, of self-consistency effects and of the interaction between neutron(s) added to a reference nucleus and the protons forming the proton subsystem, on the buildup of differential charge radii.

The paper is organized as follows. Sec. II provides a brief outline of the theoretical formalism and the discussion of physical observables under study. The role of the single-particle states forming the proton core in microscopic origin of the kinks in differential charge radii is discussed in Sec. III. Microscopic origin of the pull of neutron subshells on proton ones leading to the modifications of charge radii is discussed

in detail in Sec. IV. The limitations of the spherical shell model and the macroscopic+microscopic approach in the description of differential charge radii are briefly analyzed in Sec. V. Finally, Sec. VI summarizes the results of our paper.

II. THEORETICAL FORMALISM AND PHYSICAL OBSERVABLES

Theoretical calculations were performed within the framework of covariant density functional theory (CDFT) [22] employing the modified version of the computer code restricted to spherical symmetry used in Ref. [23]. Since the details of the CDFT framework are widely available (see, for example, Ref. [22]), we focus on the physical quantities of the interest. The pairing correlations are neglected in the calculations in order to better understand the underlying physical mechanisms. The calculations are performed with the NL3* covariant energy density functional (CEDF) [24]. Its global performance in the description of the masses and charge radii is well documented (see Refs. [3,4]). It was also recently used in the study of bubble nuclei (see Ref. [25]) the results of which have substantial overlap with some aspects of the present study; this is one of main reasons for the selection of this functional. Note that it was verified that the main conclusions obtained in the present paper do not depend on the selection of the functional.

In order to better apprehend the role of different microscopic mechanisms in building differential charge radii we consider ground state configuration in ^{208}Pb and two configurations of the ^{218}Pb nucleus labeled below as "Conf-$1i_{11/2}$" and "Conf-$2g_{9/2}$." In these configurations of ^{218}Pb, ten neutrons outside the ^{208}Pb core are located in the $1i_{11/2}$ and $2g_{9/2}$ spherical subshells, respectively. We selected ^{218}Pb in order to maximize the effect of the addition of neutrons in a given spherical subshell on proton charge radii.[1] Note that the maximum number of neutrons which can be put into the $2g_{9/2}$ and $1i_{11/2}$ spherical subshells is 10 and 12, respectively. Thus, the selection of ^{218}Pb nucleus corresponds to full filling of the $2g_{9/2}$ neutron subshell and almost (two neutrons short) full filling of the $1i_{11/2}$ neutron subshell.

The charge radii are defined as

$$r_{ch} = \sqrt{\langle r^2 \rangle_p + 0.64}\ \text{fm}, \tag{1}$$

where the mean square proton point radius is given by

$$\langle r^2 \rangle_p = \frac{\int r^2 \rho_{\text{tot}}^p(\vec{r})d^3r}{\int \rho_{\text{tot}}^p(\vec{r})d^3r} \tag{2}$$

and the factor 0.64 accounts for the finite-size effects of the proton.[2] Then the differential mean-square charge radius is

given by[3]

$$\delta\langle r^2 \rangle_p^{N,N'} = \langle r^2 \rangle_p(N) - \langle r^2 \rangle_p(N')$$
$$= r_{ch}^2(N) - r_{ch}^2(N'). \tag{3}$$

Note that N' is the neutron number of the reference nucleus (^{208}Pb in this paper).

The total nucleonic density $\rho_{\text{tot}}(r)$ in a given subsystem (proton or neutron) is built from the contributions of individual particles as follows:

$$\rho_{\text{tot}}(r) = \sum_i m_i \rho_i^{sp}(r), \tag{4}$$

where m_i is the multiplicity of the occupation of the ith subshell [$m_i = (2j_i + 1)$ for a fully occupied subshell with angular momentum j_i] and $\rho_i^{sp}(r)$ is the density of the single-particle state belonging to the ith subshell with the normalization

$$\int \rho_i^{sp}(\vec{r})d^3r = 4\pi \int r^2 \rho_i^{sp}(r)dr = 1.0. \tag{5}$$

Taking into account that $\int \rho_{\text{tot}}^p(\vec{r})d^3r = Z$ and that all proton subshells below the $Z = 82$ shell gap are fully occupied in the proton subsystem of the Pb isotopes, Eq. (2) can be rewritten as

$$\langle r^2 \rangle_p = \frac{1}{Z}\sum_i (2j_i + 1)\langle r^2 \rangle_i^p, \tag{6}$$

where

$$\langle r^2 \rangle_i^p = \int r^2 \rho_i^p(\vec{r})d^3r \tag{7}$$

is the proton mean square radius of the single-particle state belonging to the ith subshell. As a consequence, the differential charge radius of two isotopes can be redefined as

$$\delta\langle r^2 \rangle_p^{N,N'} = \frac{1}{Z}\sum_i (2j_i + 1)\big[\langle r^2 \rangle_i^p(N) - \langle r^2 \rangle_i^p(N')\big] \tag{8}$$

and its magnitude could be traced back to the modifications in proton mean square radius of the single-particle states generated by the transition from the nucleus with neutron number N' to the nucleus with neutron number N. The quantity

$$\Delta\langle r^2 \rangle_i^{N,N'} = \langle r^2 \rangle_i^p(N) - \langle r^2 \rangle_i^p(N') \tag{9}$$

_____

[1]One can definitely consider the $1i_{11/2}$ and $2g_{9/2}$ configurations in the odd-A ^{209}Pb nucleus and this will completely justify the neglect of pairing, which collapses because of the blocking of the odd neutron. However, this will not change the results and conclusions of the paper.

[2]Small contributions to the charge radii originating from the electric neutron form factor and electromagnetic spin-orbit coupling

_____

[26,27] are neglected in the NL3* functional (as well as in the fitting protocols of all existing CEDFs). More precise expressions for charge radii in CDFT are available but their use would require the refit of the CEDFs (see Refs. [28,29] and discussion in Sec. VIII of Ref. [3]). However, this neglect is not critical since spin-orbit contribution to charge radii decreases with increasing mass of nuclei [28,30] and its contribution to differential charge radii of the Pb isotopes is expected to be negligible [30].

[3]This quantity is frequently written as a function of mass number A. However, we prefer to define it as a function of neutron number N since this allows to see the behavior of the $\delta\langle r^2 \rangle_p^{N,N'}$ curves at neutron shell closures.
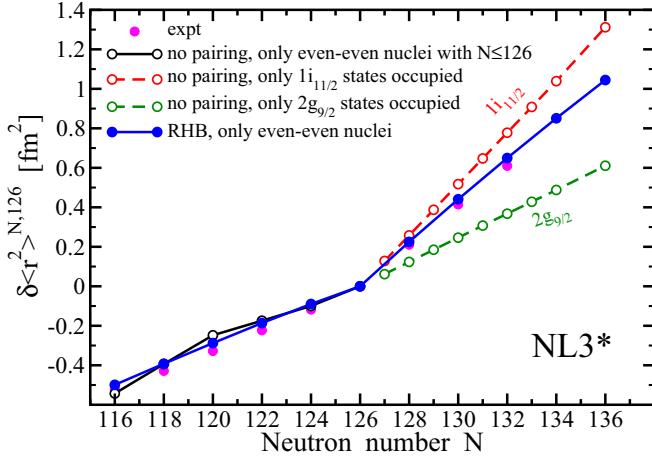
FIG. 1. The $\delta \langle r^2 \rangle^{N,126}$ values of the Pb isotopes relatively to ^{208}Pb obtained in the calculations with and without pairing.

is denoted here as differential single-particle proton radius of the single-particle state belonging to the ith proton subshell.

Note that in order to make a connection with single-particle wave functions ψ_i more straightforward, we consider single-particle rms radii r_i^p of the proton states defined as

$$r_i^p = \sqrt{\langle r^2 \rangle_i^p}. \qquad (10)$$

III. DIFFERENTIAL CHARGE RADII: THE ROLE OF THE SINGLE-PARTICLE STATES FORMING THE PROTON CORE IN MICROSCOPIC ORIGIN OF THE KINKS

It is well established in different model calculations that dominant or significant occupation of the neutron $1i_{11/2}$ subshell above the $N = 126$ shell closure is critical for explaining the kink in differential charge radii at neutron $N = 126$ shell closure [3,8,16,18,20,21,31]. The functionals (typically CEDFs) in which the $\nu 1i_{11/2}$ subshell is located below the $\nu 2g_{9/2}$ subshell reasonably well describe this kink and the slope of differential charge radii as a function of neutron number above $N = 126$. In contrast, the functionals (typically nonrelativistic ones) with opposite location of two subshells either fail to describe the kink or significantly underestimate its magnitude.

Figure 1 illustrates this situation in the CDFT calculations without pairing: the occupation of the $1i_{11/2}$ ($2g_{9/2}$) subshell above the $N = 126$ shell closure leads to an appreciable kink (no kink) in differential charge radii (see Ref. [3] for more details). The inclusion of pairing leads to partial occupation of both orbitals (see Refs. [3,31] for details) as a consequence of which the differential charge radii obtained in the relativistic Hartree-Bogoliubov (RHB) calculations become close to experimental data. Note that differential charge radii $\delta \langle r^2 \rangle_p^{136,126}$ are 1.31 and 0.61 fm^2 in the Conf-$1i_{11/2}$ and Conf-$2g_{9/2}$ configurations of ^{218}Pb, respectively.

The detailed investigation of self-consistency effects related to the changes of proton potential, total proton and neutron densities, and relevant changes in the single-particle

energies on the transition from the ground state of the ^{208}Pb nucleus to the Conf-$1i_{11/2}$ and Conf-$2g_{9/2}$ configurations in ^{218}Pb reveals that they provide only minor contribution to respective differential charge radii.

Thus, the buildup of differential charge radii as a function of neutron number is related to the occupation of respective neutron single-particle states and their interaction with proton ones. To better understand the microscopic mechanisms leading to such large differences, we show in Tables I and II the contributions of different spherical subshells into buildup of differential charge radii of the Conf-$1i_{11/2}$ and Conf-$2g_{9/2}$ configurations of ^{218}Pb.

Table I clearly shows that when the neutron $1i_{11/2}$ subshell is occupied in ^{218}Pb the largest changes in proton single-particle rms radii δr_i^p take place for proton subshells with principal quantum number $n = 1$. The δr_i^p values for the s, p, and d $n = 2$ subshells are smaller than the average δr_i^p value over the $n = 1$ subshells by factors of approximately 2, 5, and 25, respectively. The proton single-particle rms radius of the $3s_{1/2}$ subshell even decreases on transition from the ground state configuration of ^{208}Pb to the Conf-$1i_{11/2}$ configuration of ^{218}Pb. All these changes are reflected also in differential single-particle proton radii $\Delta \langle r^2 \rangle_i^{N,N'}$ (see column 7 of Table I) so that 96.7% of differential charge radius $\delta \langle r^2 \rangle_p^{136,126} = 1.31$ fm^2 [see Eq. (3)] of the Conf-$1i_{11/2}$ configuration in ^{218}Pb with respect of the ground state configuration in ^{208}Pb are built by the $n = 1$ proton subshells.

The situation drastically changes when the neutron $2g_{9/2}$ subshell is occupied in ^{218}Pb (configuration Conf-$2g_{9/2}$); see Table II. In this case, the largest δr_i^p values are seen for the $2s_{1/2}$, $2p_{3/2}$, $2p_{1/2}$, $2d_{5/2}$. and $2d_{3/2}$ proton subshells. The proton rms radii of low lying $1s_{1/2}$, $1p_{3/2}$, $1p_{1/2}$, $1d_{5/2}$, and $1d_{3/2}$ subshells even decrease on transition from the ground state configuration of ^{208}Pb to the Conf-$2g_{9/2}$ configuration of ^{218}Pb. In addition, the increase of proton rms radii is rather modest for remaining $n = 1$ subshells and for the $3s_{1/2}$ subshell. All these changes are reflected also in differential single-particle proton radii $\Delta \langle r^2 \rangle_i^{N,N'}$ (see column 7 of Table II) so that 53.3% of differential charge radius $\delta \langle r^2 \rangle_p^{136,126} = 0.61$ fm^2 of two configurations under study are built by the $n = 2$ proton subshells. This is despite the low multiplicity of the occupied $n = 2$ subshells which represents only approximately 22% of the occupied single-particle states of the $Z = 82$ core.

The impact of the occupation of neutron $2g_{9/2}$ subshell on proton single-particle rms radii of the $n = 2$ proton subshells (see Table II) is on average comparable to the one of the neutron $1i_{11/2}$ subshell on proton single-particle rms radii of the $n = 1$ proton subshells (see Table I). Thus, other factors have to be involved to explain large difference in differential charge radii of the Conf-$1i_{11/2}$ and Conf-$2g_{9/2}$ configurations in ^{218}Pb. Indeed, the analysis of Eq. (8) clearly indicates that differential charge radii between two isotopes are defined not only by the differential single-particle radii $\Delta \langle r^2 \rangle_i^{N,N'}$ of occupied single-particle states but also by the abundance of the subshells with a given n among occupied subshells and their multiplicity m_i. Low n subshells are most abundant in any nucleonic potential (see Refs. [25,32]). Indeed, there are

TABLE I. The contributions of different spherical subshells (column 7) to the buildup of differential charge radii of the Conf-$1i_{11/2}$ configuration in ^{218}Pb. The ground state configuration in ^{208}Pb is used here as a reference. Proton subshells occupied below the $Z = 82$ shell closure are shown in column 1. Their single-particle energies e_i (in MeV) are shown in columns 2 and 3 for two configurations under study. Their proton single-particle rms radii r_i^p are displayed in columns 4 and 5. The column 6 shows the change of proton single-particle radii $\delta r_i^p = r_i^p(^{218}\text{Pb[Conf-}1i_{11/2}]) - r_i^p(^{208}\text{Pb})$. Column 7 shows differential single-particle proton radii $\Delta\langle r^2\rangle_i^{N,N'}$ of the single-particle state belonging to the ith proton subshell. The overlaps of proton and neutron wave functions $\langle\Psi_n^k|\Psi_p^i\rangle$ are shown in column 8. The results for spherical subshells with principal quantum number $n = 1$ are shown in bold. The total quantities given in the last line are calculated using Eq. (8) (column 7) and equations similar to it (columns 4, 5, and 6).

Subshell	$e_i(^{208}\text{Pb})$	$e_i(^{218}\text{Pb})$	$r_i^p(^{208}\text{Pb})$	$r_i^p(^{218}\text{Pb})$	δr_i^p	$\Delta\langle r^2\rangle_i^{N,N'}$	$\langle\Psi_n^k|\Psi_p^i\rangle$
1	2	3	4	5	6	7	8
$1s_{1/2}$	**−48.905**	**−48.271**	**4.064254**	**4.235252**	**0.170998**	**1.419199**	**0.570778**
$1p_{3/2}$	**−43.211**	**−43.156**	**4.663197**	**4.846186**	**0.182989**	**1.740112**	**0.729091**
$1p_{1/2}$	**−42.529**	**−42.598**	**4.582763**	**4.771297**	**0.188534**	**1.763556**	**0.694871**
$1d_{5/2}$	**−36.118**	**−36.727**	**5.105879**	**5.283008**	**0.177129**	**1.840178**	**0.795503**
$1d_{3/2}$	**−34.559**	**−35.462**	**4.981504**	**5.159900**	**0.178396**	**1.809189**	**0.795142**
$2s_{1/2}$	−30.886	−32.032	4.450498	4.528233	0.077735	0.697962	−0.638347
$1f_{7/2}$	**−28.068**	**−29.330**	**5.479627**	**5.643146**	**0.163519**	**1.818783**	**0.899794**
$1f_{5/2}$	**−25.298**	**−27.044**	**5.334254**	**5.490660**	**0.156406**	**1.693085**	**0.837178**
$2p_{3/2}$	−20.924	−22.559	4.985584	5.017296	0.031712	0.317213	−0.571543
$2p_{1/2}$	−19.865	−21.566	5.004156	5.031929	0.027773	0.278730	−0.583835
$1g_{9/2}$	**−19.396**	**−21.242**	**5.816346**	**5.962968**	**0.146622**	**1.727100**	**0.910026**
$1g_{7/2}$	**−15.205**	**−17.693**	**5.682103**	**5.807857**	**0.125754**	**1.444908**	**0.932110**
$2d_{5/2}$	−11.163	−13.089	5.522224	5.527597	0.005373	0.059372	−0.521033
$1h_{11/2}$	**−10.360**	**−12.684**	**6.129798**	**6.257349**	**0.127551**	**1.579994**	**0.975584**
$2d_{3/2}$	−9.513	−11.537	5.580005	5.584444	0.004439	0.049559	−0.554369
$3s_{1/2}$	−8.405	−10.360	5.489444	5.476911	−0.012533	−0.137438	0.448467
Total			5.450221	5.569299	0.119078	1.312261	

ten $n = 1$, five $n = 2$, and one $n = 3$ occupied subshells in the $Z = 82$ core of the Pb isotopes (see Table I). In addition, the $n = 1$ subshells have the highest multiplicity m_{max} among the occupied subshells: $m_{\text{max}} = 12$, 6, and 2 for the $n = 1$, 2, and 3 subshells, respectively. As a result, 62, 18, and 2 protons of the $Z = 82$ core are located in the $n = 1$, 2, and 3 subshells, respectively. The combination of all above mentioned in this subsection factors allows to explain large difference in differential charge radii of the Conf-$1i_{11/2}$ and Conf-$2g_{9/2}$ configurations in ^{218}Pb.

TABLE II. The same as in Table I but for the Conf-$2g_{9/2}$ configuration in ^{218}Pb. The results for spherical subshells with principal quantum number $n = 2$ are shown in bold. Note that δr_i^p in column 6 is defined as $\delta r_i^p = r_i^p(^{218}\text{Pb[Conf-}2g_{9/2}]) - r_i^p(^{208}\text{Pb})$.

| Subshell	$e_i(^{208}\text{Pb})$	$e_i(^{218}\text{Pb})$	$r_i^p(^{208}\text{Pb})$	$r_i^p(^{218}\text{Pb})$	δr_i^p	$\Delta\langle r^2\rangle_i^{N,N'}$	$\langle\Psi_n^k|\Psi_p^i\rangle$
1	2	3	4	5	6	7	8
$1s_{1/2}$	−48.905	−50.239	4.064254	4.062288	−0.001966	−0.015978	0.399380
$1p_{3/2}$	−43.211	−44.539	4.663197	4.631773	−0.031424	−0.292086	0.345824
$1p_{1/2}$	−42.529	−43.915	4.582763	4.535377	−0.047386	−0.432074	0.373550
$1d_{5/2}$	−36.118	−37.305	5.105879	5.092180	−0.013699	−0.139704	0.273309
$1d_{3/2}$	−34.559	−35.720	4.981504	4.962466	−0.019038	−0.189316	0.282916
$2s_{1/2}$	**−30.886**	**−31.484**	**4.450498**	**4.565793**	**0.115295**	**1.039534**	**0.182596**
$1f_{7/2}$	−28.068	−29.174	5.479627	5.496088	0.016461	0.180670	0.119881
$1f_{5/2}$	−25.298	−26.329	5.334254	5.363151	0.028897	0.309126	0.186386
$2p_{3/2}$	**−20.924**	**−22.315**	**4.985584**	**5.158503**	**0.172919**	**1.754108**	**0.475303**
$2p_{1/2}$	**−19.865**	**−21.544**	**5.004156**	**5.170061**	**0.165905**	**1.687954**	**0.447216**
$1g_{9/2}$	−19.396	−20.544	5.816346	5.862341	0.045995	0.537159	−0.000955
$1g_{7/2}$	−15.205	−16.330	5.682103	5.757601	0.075498	0.863670	−0.000587
$2d_{5/2}$	**−11.163**	**−13.214**	**5.522224**	**5.663334**	**0.14111**	**1.578392**	**0.754258**
$1h_{11/2}$	−10.360	−11.659	6.129798	6.199679	0.069881	0.861599	−0.182783
$2d_{3/2}$	**−9.513**	**−11.887**	**5.580005**	**5.686162**	**0.106157**	**1.195982**	**0.719801**
$3s_{1/2}$	−8.405	−10.335	5.489444	5.540033	0.050589	0.557970	−0.7388235
Total			5.450221	5.505978	0.055757	0.6110	
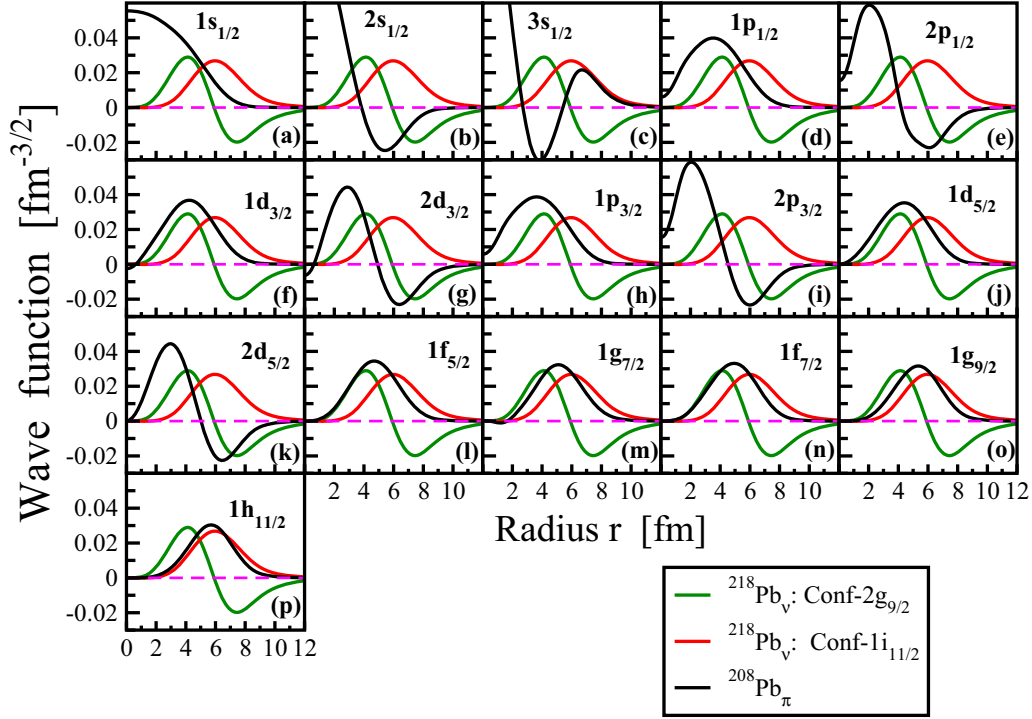
FIG. 2. Single-particle wave functions of proton (black curves) spherical subshells in ^{208}Pb nucleus compared with those of the neutron $2g_{9/2}$ (green lines) and $1i_{11/2}$ (red lines) subshells. Note that the latter two states are shown in each panel. Proton subshell labels are shown on each panel. The wave functions Ψ_i of the proton $2s_{1/2}$ and $3_{1/2}$ states [see panels (b) and (c)] in the ^{208}Pb nucleus gradually increase above 0.06 fm$^{-3/2}$ (upper limit on vertical axis) with decreasing radius r and reach $\Psi_{2s_{1/2}} \approx 0.115$ fm$^{-3/2}$ and $\Psi_{3s_{1/2}} \approx 0.138$ fm$^{-3/2}$ at $r = 0$, respectively.

IV. MICROSCOPIC ORIGIN OF THE PULL OF NEUTRON SUBSHELLS ON PROTON ONES

In order to better understand the state dependence of the pull provided by a neutron in a given state on the proton in the nlj subshell, Fig. 2 compares the proton wave functions of all occupied proton subshells in the $Z = 82$ core of the ^{208}Pb nucleus with the neutron wave functions of the neutron $1i_{11/2}$ and $2g_{9/2}$ subshells calculated in the Conf-$1i_{11/2}$ and Conf-$2g_{9/2}$ configurations of ^{218}Pb, respectively. In addition, the overlap of respective proton and neutron wave functions defined as

$$\langle \Psi_n^k | \Psi_p^i \rangle = \int \Psi_n^k(\vec{r}) \Psi_p^i(\vec{r}) d^3r \qquad (11)$$

is presented in the last columns of Tables I and II. Here proton state index i runs over all occupied proton subshells while neutron index k is either $k = 1i_{11/2}$ or $k = 2g_{9/2}$. Positive (negative) values of these overlaps indicate that the wave functions Ψ_n^k and Ψ_p^i are spatially mostly in phase (out of phase).

Let us first consider the overlaps of proton wave functions with the neutron $\nu 1i_{11/2}$ one [see Table I]. The largest overlap exists for the $\pi 1h_{11/2}$ state ($\langle \Psi_n^k | \Psi_p^i \rangle = 0.98$). Indeed, these two states have the wave functions which are most similar among considered cases [see Fig. 2(p) and compare it with other panels of this figure]. The degree of the similarity ($\langle \Psi_n^k | \Psi_p^i \rangle \approx 0.92$) of the wave function of the neutron $\nu 1i_{11/2}$ subshell is somewhat smaller with the wave functions of the

proton $\pi 1g_{7/2}$ and $\pi 1g_{9/2}$ subshells [see Figs. 2(m) and 2(o)]. With decreasing single-particle energy of the spherical $n = 1$ proton subshell, the degree of the similarity between neutron and proton wave functions given by $\langle \Psi_n^k | \Psi_p^i \rangle$ decreases but still remains high (see the last column of Table I and Figs. 2(l), 2(j), 2(h), 2(f), 2(d), and 2(a)]. Among the proton $n = 1$ subshells the lowest overlap $\langle \Psi_n^k | \Psi_p^i \rangle = 0.57$ exists for the proton $1s_{1/2}$ subshell which is the only $n = 1$ subshell with the maximum of the wave function at the center of the nucleus [see Fig. 2(a)].

The situation is completely different for the proton subshells with $n = 2$: the evolution of their wave functions as a function of radial coordinate r is mostly out of phase with that of the wave function of the neutron $1i_{11/2}$ subshell [see Figs. 2(b), 2(e), 2(g), 2(i), and 2(k)]. This is due to the differences in the nodal structure of these wave functions. As a consequence, large negative overlaps $\langle \Psi_n^k | \Psi_p^i \rangle$ exist for these pairs of states (see last column of Table I). There are large differences due to underlying nodal structure between the wave functions of the proton $3s_{1/2}$ and neutron $1i_{11/2}$ subshells [see Fig. 2(c)]. However, the overlap $\langle \Psi_n^k | \Psi_p^i \rangle$ for this pair of subshells is positive due to the fact that the overlap is dominated by the behavior of the wave functions at large radial coordinates.

The occupation of neutron $2g_{9/2}$ subshell leads to a completely different pattern of behavior (see Fig. 2 and Table II). The largest overlaps exist for the $n = 2$ proton subshells: the only exception is the overlap which includes the proton $2s_{1/2}$
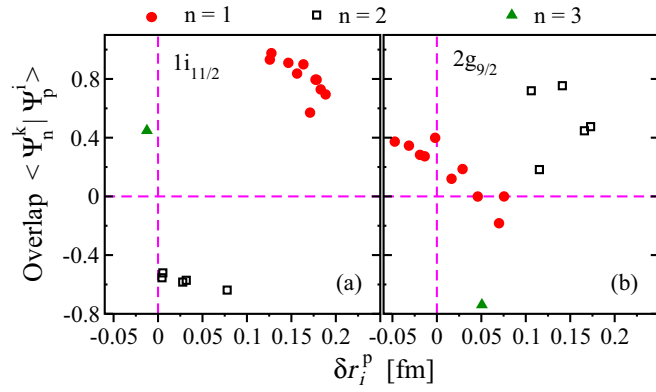
FIG. 3. The correlations between the overlaps $\langle\Psi_n^k|\Psi_p^i\rangle$ and the changes of proton single-particle radii δr_i^p for proton subshells of the $Z = 82$ core. Solid red circles, open black squares, and green triangles are used for the $n = 1$, $n = 2$, and $n = 3$ proton subshells. Panels (a) and (b) show the results when neutron $1i_{11/2}$ and $2g_{9/2}$ subshells are occupied in the configurations of the ^{218}Pb nucleus, respectively. Note that similar correlations are also seen between $\langle\Psi_n^k|\Psi_p^i\rangle$ and differential single-particle proton radii $\Delta\langle r^2\rangle_i^{N,N'}$.

subshell, which has a maximum of its wave function at $r = 0$. These overlaps become smaller or even negative for the cases which include $n = 1$ and $n = 3$ proton subshells (see the last column in Table II).

Figure 3 shows the correlations between the overlaps $\langle\Psi_n^k|\Psi_p^i\rangle$ for the neutrons in the $1i_{11/2}$ and $2g_{9/2}$ subshells and the proton subshells occupied in the $Z = 82$ core and the changes in single-particle proton rms radii δr_i^p of these subshells triggered by the occupation of respective neutron subshells. In general, the largest δr_i^p values appear for the proton subshells which have the same principal quantum number n as the occupied neutron subshell. This also corresponds to the largest positive overlaps $\langle\Psi_n^k|\Psi_p^i\rangle$. Small or negative overlaps, which correspond to the case of different principal quantum numbers n of proton and neutron subshells, typically lead to relatively small δr_i^p values.

These correlations are very pronounced in the case of the occupation of the neutron $1i_{11/2}$ subshell since its wave function has a simple structure with a single maximum at $r \approx 6$ fm (see Fig. 2). Significant changes in the single-particle rms radius are seen for proton $n = 1$ subshells which have large overlaps $\langle\Psi_n^k|\Psi_p^i\rangle$, but rather small δr_i^p values exist for proton $n = 2$ subshells which have negative overlaps [see Fig. 3(a) and Table I].

Such correlations are somewhat less pronounced in the case of the occupation of the $2g_{9/2}$ neutron subshell, the wave function of which has its maximum at $r \approx 4$ fm and minimum at $r = 7.5$ fm (see Fig. 2). The largest overlaps $\langle\Psi_n^k|\Psi_p^i\rangle$ are seen with proton $n = 2$ $2p_{3/2}$, $2p_{1/2}$, $2d_{5/2}$, and $2d_{3/2}$ subshells which produce the largest changes in the proton single-particle rms radii (see Fig. 3 and Table II). Smaller and sometimes negative changes in the proton single-particle rms radii are produced for the $n = 1$ and $n = 3$ proton subshells when the neutron $2g_{9/2}$ subshell becomes occupied.

The absolute values of the $\langle\Psi_n^k|\Psi_p^i\rangle$ overlaps presented in column 8 of Tables I and II are similar to those obtained in

Skyrme DFT calculations with the NRAPRii energy density functional (see Fig. 5 of Ref. [21]). This clearly indicates a similar mechanism of the buildup of differential charge radii in nonrelativistic and covariant DFTs. However, our analysis below shows that the sign of the $\Psi_n^k(r)\Psi_p^i(r)$ product (and, as a consequence, of the $\langle\Psi_n^k|\Psi_p^i\rangle$ overlaps) is important for an understanding of the impact of the occupation of a specific neutron subshell on the radii of proton orbitals forming the $Z = 82$ core. There is also a difference in the interpretation of the source of these modifications in charge radii caused by the occupation of different neutron subshells and increasing neutron number between the present paper and Ref. [21]. Strong nuclear symmetry energy is indicated as a source of these changes in Ref. [21]. In contrast, our detailed analysis clearly indicates that they are due to proton-neutron interaction. This is similar to the fact that proton-neutron interaction plays a dominant role in building the deformation (see Refs. [33,34] for details).

Because of the dependence of charge radii and their changes on proton single-particle densities (see Sec. II), a deeper microscopic insight is provided by the analysis of the redistributions of the proton single-particle densities, defined as

$$\delta\rho_i^p(r) = \rho_i^p(r)[^{218}\text{Pb -conf}] - \rho_i^p(r)[^{208}\text{Pb}] \qquad (12)$$

when different neutron subshells are occupied in ^{218}Pb. Since the single-particle density is normalized to unity [see Eq. (5)], the addition of neutron(s) to the ^{208}Pb nucleus will only lead to redistribution of the proton single-particle density under the condition that

$$\int r^2 \delta\rho_i^p(r) = 0. \qquad (13)$$

These redistributions are shown in Fig. 4. Let us consider as an example the changes in the single-particle proton densities of the $1p_{3/2}$ subshell [see Fig. 4(h)]. The occupation of the neutrons in the $2g_{9/2}$ subshell (the Conf-$2g_{9/2}$ configuration in ^{218}Pb) leads to an increase of proton densities of the $1p_{3/2}$ subshell at $r \approx 3.2$ fm and their decrease at $r \approx 5.5$ fm as compared with that in the ground state configuration of ^{208}Pb [green line in Fig. 4(h)]. In contrast, the occupation of the neutrons in the $1i_{11/2}$ subshell (the Conf-$1i_{11/2}$ configuration in ^{218}Pb) has an opposite effect: it leads to the decrease of proton densities of the $1p_{3/2}$ subshell at $r \approx 3$ fm and their increase[4] at $r \approx 6$ fm [red line in Fig. 4(h)]. Note that the number of the oscillations of density redistributions increases with the increase of principal quantum number n of the proton and neutron subshells involved [compare, for example, the panels (c) and (h) of Fig. 4].

---

[4]The reader should not be confused by larger density changes at low radial coordinates as compared with those at larger values of r. This is because the density plots as a function of radial coordinate tend to overemphasize the importance of the central region since they ignore the fact that the number of particles dn in a spherical shell of thickness dr is given by $4\pi r^2\rho(r)dr$ (see the example in Sec. III of Ref. [25]).
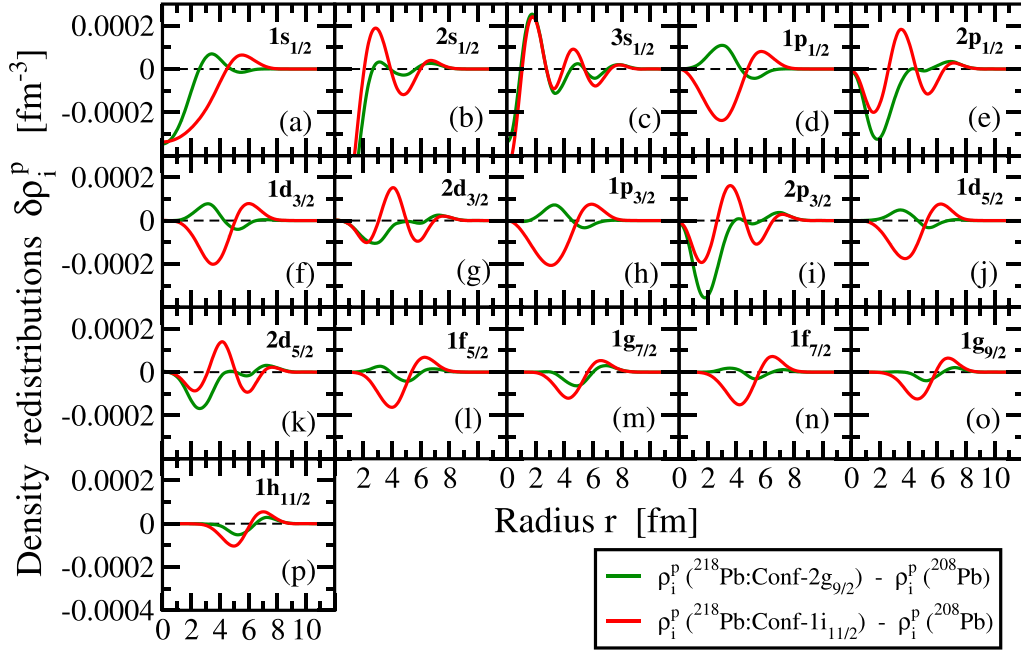
FIG. 4. Proton single-particle density redistributions $\delta\rho_i^p(r)$ caused by the occupation of indicated neutron subshells in ^{218}Pb (see text for details). Note that the density redistributions are very similar for the spin-orbit partner states [compare panels (d) and (h), (e) and (i), (f) and (j), (g) and (k), (l) and (n), (m) and (o)].

For almost all proton subshells of the $Z = 82$ core the occupation of the $1i_{11/2}$ or $2g_{9/2}$ neutron subshells leads to drastically different redistributions of proton single-particle densities which are frequently out of phase with each other as a function of radial coordinate r (see Fig. 4). Thus, for a given proton subshell this leads to different changes in the proton single-particle radii δr_i^p and substantial differences in differential single-particle radii $\Delta\langle r^2\rangle_i^{N,N'}$ (compare Tables I and II).

One can ask which microscopic physical processes are driving these density redistributions, which factors affect them, and why these redistributions are different for the occupation of the neutron $1i_{11/2}$ and $2g_{9/2}$ neutron subshells. To answer these questions the density redistributions $\rho_i^p(^{218}$Pb: Conf-$1i_{11/2}) - \rho_i^p(^{208}$Pb) caused by the occupation of the $1_{11/2}$ neutron subshell are compared with radial profiles of single-particle densities ρ_i^p of the proton states in the $Z = 82$ core and the $\Psi_n^{1i_{11/2}}(r)\Psi_p^i(r)$ products of the single-particle wave functions in Fig. 5.

The situation is the simplest in the cases of the $n = 1$ $l > 1$ proton orbitals such as $1d_{3/2}$, $1d_{5/2}$, $1f_{5/2}$, $1f_{7/2}$, $1g_{7/2}$, $1g_{9/2}$, and $1h_{11/2}$ [see Figs. 5(f), 5(j), 5(l), 5(n), 5(m), 5(o), and 5(p), respectively]. This is because (i) interacting proton and neutron $n = 1$ orbitals do not have a node in their wave functions and (ii) the maxima of $\rho_i^p(r)$ and $\Psi_n^{1i_{11/2}}(r)\Psi_p^i(r)$ are located reasonably close to each other in radial coordinate. In all these cases the proton matter is moved from inside of the nucleus [typically from the $r < r_0$ region in which $\Psi_n^{1i_{11/2}}(r)\Psi_p^i(r)$ increases with increasing radial coordinate] towards surface region (typically into the $r > r_0$ region in

which $\Psi_n^{1i_{11/2}}(r)\Psi_p^i(r)$ decreases with increasing radial coordinate) [see Figs. 5 and 6(a)]. Here, r_0 is the r value at which $\rho_i^p(^{218}$Pb: Conf-$1i_{11/2}) - \rho_i^p(^{208}$Pb) $= 0$. It is located between 5 and 6 fm for the $n = 1$ $l > 1$ proton orbitals. Note that in all these cases the maxima of the $\Psi_n^{1i_{11/2}}(r)\Psi_p^i(r)$ products are located close to r_0.

Similar features also hold for the $n = 1$ $1s_{1/2}$, $1p_{1/2}$ and $1p_{3/2}$ orbitals [see Figs. 5(a), 5(d), and 5(h)]. However the density redistributions $\rho_i^p(^{218}$Pb: Conf-$1i_{11/2}) - \rho_i^p(^{208}$Pb) become less symmetric in radial coordinate and the maxima of the $\Psi_n^{1i_{11/2}}(r)\Psi_p^i(r)$ products deviate more strongly from r_0. This is in part due to the fact that the maxima of the $\Psi_n^{1i_{11/2}}(r)\Psi_p^i(r)$ products are shifted towards the tail of the single-particle densities $\rho_i^p(r)$. In addition, the $\rho_i^p(r)$ maximum of the $l = 0$, $1s_{1/2}$ state is located at $r = 0$.

The situation becomes more complex for the $n = 2$ and $n = 3$ proton subshells. First of all, these states have one (at $r_1^{n=2}$) and two nodes (at $r_1^{n=3}$ and at $r_2^{n=3}$) in their wave functions [see Figs. 2(b), 2(c), 2(e), 2(g), 2(i), and 2(k)], respectively, which are also seen in the single-particle density distributions ρ_i^p in Figs. 5(c), 2(e), 2(g), 2(i), and 2(k). For example, $r_1^{n=2} \approx 4.2$ fm for the $2p_{1/2}$ state [see Figs. 2(e) and 5(e)] and $r_1^{n=3} \approx 2.8$ fm and $r_2^{n=3} \approx 5.4$ fm for the $3s_{1/2}$ state [see Figs. 2(c) and 5(c)]. Proton density redistributions $\rho_i^p(^{218}$Pb: Conf-$1i_{11/2}) - \rho_i^p(^{208}$Pb) are also zero at these coordinates [Figs. 5(c), 5(e), 5(g), 5(i), and 5(k)].

It is important to understand how the proton density redistribution works in the cases of the proton states with one and two nodes in the wave function. To achieve that a detailed analysis of the proton density redistributions of the
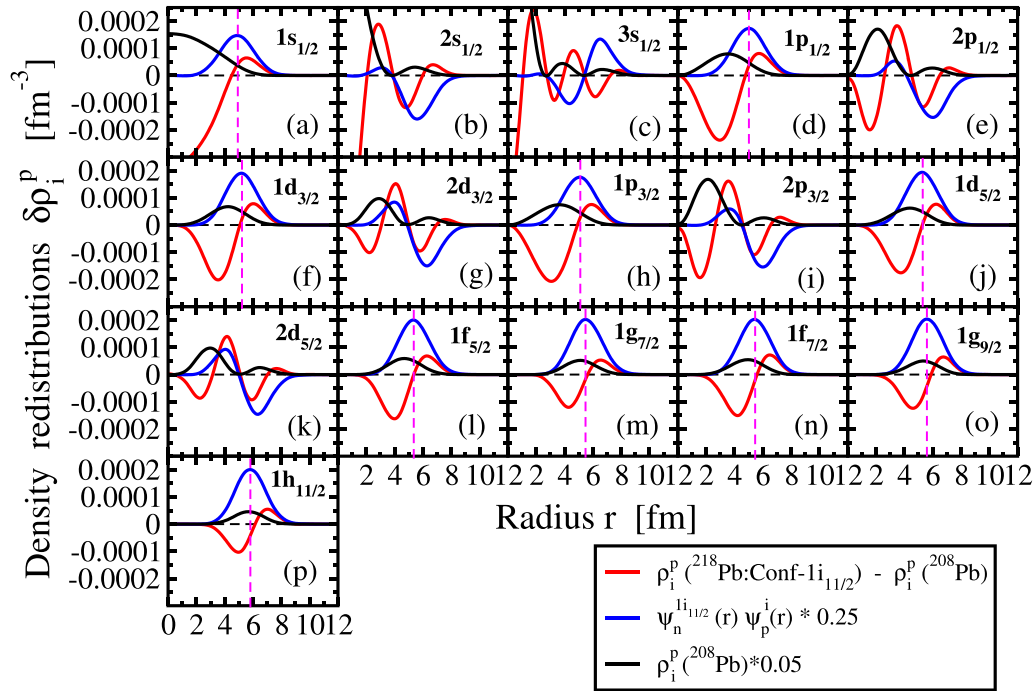
FIG. 5. Proton single-particle density redistributions $\delta\rho_i^p(r)$ caused by the occupation of the neutron $1i_{11/2}$ subshell in ^{218}Pb compared with single-particle densities $\rho_i^p(r)$ of indicated proton states in the $Z = 82$ core and the $\Psi_n^{1i_{11/2}}(r)\Psi_p^i(r)$ products. Note that, in order to fit them into the figure, the latter two quantities are multiplied by factors 0.05 and 0.25, respectively. Vertical pink dashed lines indicate the radial coordinate at which $\Psi_n^{1i_{11/2}}(r)\Psi_p^i(r)$ products have a maximum for the $n = 1$ proton subshells.

proton $2d_{3/2}$ and $3s_{1/2}$ states is presented based on Fig. 6 and Table III. To facilitate the discussion we define the sectors in radial coordinate. These are

sector (i) between the center ($r = 0$) of the nucleus and $r_1^{n=2}$ and

sector (ii) between $r_1^{n=2}$ and the surface of the nucleus

for the $n = 2$ states [see Fig. 6(b)] and

sector (i) between the center ($r = 0$) of the nucleus and $r_1^{n=3}$,

sector (ii) between $r_1^{n=3}$ and $r_2^{n=3}$, and

sector (iii) between $r_2^{n=3}$ and the surface of the nucleus

for the $n = 3$ states [see Fig. 6(c)].

In each sector there are the regions of radial coordinate with $\delta\rho_i^p < 0$ and $\delta\rho_i^p > 0$ which are labeled as A and B, respectively. This is illustrated in Fig. 6(b). So during the proton density redistribution process caused by the occupation
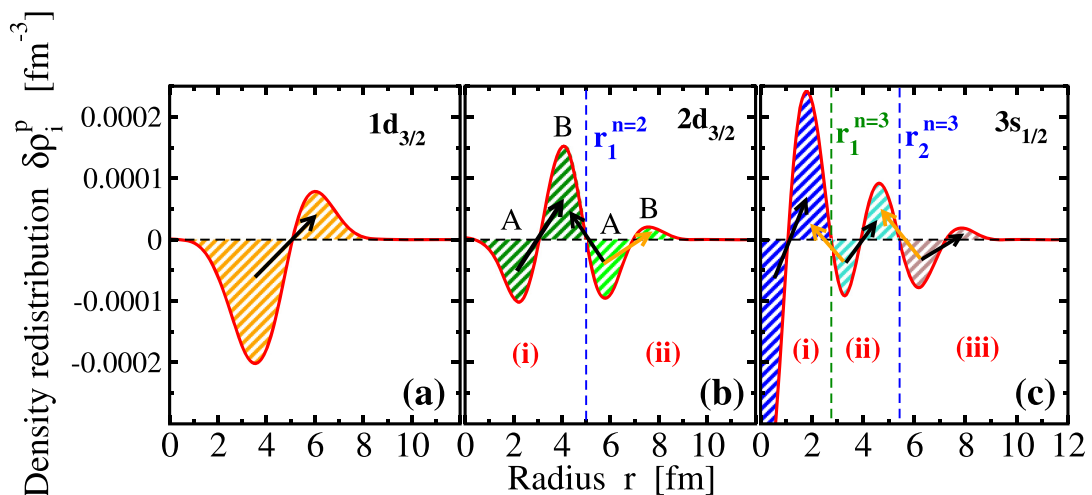

FIG. 6. Density redistributions $\delta\rho_i^p$ in the case of the indicated $n = 1$, 2, and 3 proton states. Vertical dashed lines in the cases of the $n = 2$ and 3 states show the positions of the nodes. See text for details.

TABLE III. The amount of proton matter m (normalized to a single state) redistributed in the regions A and B of the states shown in panels (a)–(c) of Fig. 6.

Panel	Sector	Region		A+B
		A	B	
(a)		−0.065345	0.065345	0
(b)	(i)	−0.007288	0.037636	0.030348
	(ii)	−0.049197	0.018849	−0.030348
(c)	(i)	−0.000801	0.011598	0.010797
	(ii)	−0.008342	0.023059	0.014717
	(iii)	−0.041636	0.016122	−0.025514

of neutron state the proton matter m moves between these regions. Its amount (per state) moved from/to region A/B can be defined as

$$m = 4\pi \int_{r_{\text{low}}}^{r_{\text{high}}} r^2 \delta\rho_i^p(r), \qquad (14)$$

where r_{low} and r_{high} are the lowest and highest radial coordinates of respective region. These values are tabulated in Table III for the states shown in Fig. 6. One can see that proton matter transfer takes place not only between regions A and B of a given sector but also between different sectors. The dominant/secondary mass transfers from regions A to regions B are shown by black/orange arrows in Figs. 6. For example, proton matter in region B of sector (i) in Fig. 6(b) is built by moving it from region A of sector (i) and from region A of sector (ii). This is the dominant process since only a relatively small amount of proton matter is moved from region A of sector (ii) to region B of the same sector.

The analysis of Table III and Fig. 6 reveals a principal difference in the redistribution of proton density and its impact on charge radii between the $n = 1$ and higher n proton states. In the case of the $n = 1$ proton states the interaction with the neutron $1i_{11/2}$ state always moves proton matter from the inner to outer region of the nucleus [see, for example, Fig. 6(a)]. This leads to a substantial increase of charge radii (see Table I). In contrast, the matter is partially moved locally to lower radial coordinates in the case of the $n = 2$ and 3 states [see Figs. 6(b) and 6(c)]. This leads to a substantially lower increase of charge radii or even to its decrease as in the case of the $3s_{1/2}$ subshell (see Table I).

The present analysis clearly indicates that proton single-particle density redistributions $\delta\rho_i^p(r)$ are caused by the proton-neutron interaction which is defined by the $\Psi_n^{1i_{11/2}}(r)\Psi_p^i(r)$ products. The outcome of this process depends in a complicated way (especially for the cases when neutron subshell has $n \geqslant 2$) on the radial profiles of these products and single-particle densities $\rho_i^p(r)$ and their nodal structure. Note that $\rho_i^p(r)$ defines how much proton matter is available at coordinate r for redistribution to another coordinate. The present analysis also shows that not only the magnitude but also the sign of the $\Psi_n^{1i_{11/2}}(r)\Psi_p^i(r)$ product is important for an understanding of how proton matter at a given radial coordinate is redistributed by the proton-neutron interaction.

Similar processes are also active in the case of the occupation of the neutron $2g_{9/2}$ subshell. In this case only $n = 2$ proton and neutron states interact in a coherent manner because of similar spatial distribution of their wave functions. This leads to large values of the $\Psi_n^{2g_{9/2}}(r)\Psi_p^i(r)$ products and significant increases in differential single-particle proton radii (see Table II). When one deals with the interaction of the proton $n = 1$ states with neutron $n = 2$ $2g_{9/2}$ ones in the case of the occupation of the $2g_{9/2}$ neutron subshell, the situation is very similar to that seen when proton $n = 2$ states interact with $n = 1$ $1i_{11/2}$ ones discussed above. In both cases there is a substantial difference in the radial profiles of the $\Psi_n^{1i_{11/2}}(r)\Psi_p^i(r)$ and $\rho_i^p(r)$ which leads to a quite modest increase (or even decrease in some cases) of single-particle proton radii (see Tables I and II).

V. APPLICABILITY OF ALTERNATIVE MODELS TO THE DESCRIPTION OF DIFFERENTIAL CHARGE RADII

As reviewed in the introduction of Ref. [3], the absolute majority of the studies of differential charge radii have been performed either in the DFT or in *ab initio* approaches. However, it is well known that the DFT models have some deficiencies in the description of spectroscopic properties related to the energies of the single-particle states and their wave functions [35–39]. Moreover, the performance of *ab initio* models in the description of single-particle spectra in odd-A nuclei is comparable with that for the DFT models, but such calculations are available only for light nuclei (see Refs. [40–43]). In contrast, spherical shell models with empirical interactions provide a better description of experimental spectroscopic data in spherical nuclei located in the vicinity of doubly magic nuclei, and microscopic+macroscopic (mic+mac) models based on phenomenological potentials such as the Woods-Saxon one do the same in the region of deformed nuclei. However, these models are not expected to be adequate for the description of differential charge radii due to the reasons mentioned below.

Although the spherical shell model takes into account the proton-neutron interaction, it suffers from the introduction of the core. As a consequence, the pull provided by neutron(s) on the proton single-particle states forming the core, the microscopic origin of which is discussed in Sec. IV, is ignored and this affects drastically the calculated charge radii of the nuclei with valence nucleons outside the core. This introduces uncontrollable errors in the calculations of differential charge radii and thus severely limits the applicability of spherical shell model to the description of this observable. A few existing calculations of differential charge radii using the spherical shell model (see Refs. [44,45]) suffer from this problem. For example, they cannot reproduce the kink in the differential charge radii of the Sn isotopes at $N = 82$ and Pb isotopes at $N = 126$ [45]. This problem can be rectified by employing the no-core shell model but because of numerical reasons such models are applicable only to light nuclei [46,47].

Phenomelogical Nilsson and Wood-Saxon potentials have been used for the description of differential charge radii in the

past (see, for example, Refs. [48,49]). However, the lack of self-consistency effects and the interaction between protons and neutrons will lead to uncontrollable errors in the models based on these potentials. This is because in these models the addition of neutrons does not affect the proton subsystem in a self-consistent manner on the level of single-particle subshells via the mechanisms discussed in Secs. III and IV. This means that the occupation of the neutron $1i_{11/2}$ and $2g_{9/2}$ subshells in the $N > 126$ Pb isotopes will lead to the same differential charge radii, contrary to the results of self-consistent calculations (see Fig. 1 and Refs. [3,8,18]).

VI. CONCLUSIONS

The self-consistency and proton-neutron interaction effects in the buildup of differential charge radii were considered by comparing two configurations of the ^{218}Pb nucleus, generated by the occupation of the neutron $1i_{11/2}$ and $2g_{9/2}$ subshells, with the ground state configuration in ^{208}Pb. The main contribution to differential charge radii has a single-particle origin and comes from the interaction of added neutron(s) and the

protons forming the $Z = 82$ proton core. This proton-neutron interaction depends on the products of proton and neutron wave functions and leads to a redistribution of single-particle density of occupied proton states which in turn modifies the charge radii. Its impact is similar to the case of building nuclear deformation which is primarily driven by proton-neutron interaction both in the nuclear shell model [50] and in DFTs [33,34]. In contrast, self-consistency effects affecting the shape of proton potential, proton densities, and the energies of the single-particle states in the proton potential provide only a small contribution. Note that the buildup of differential charge radii between two isotopes is also a collective phenomenon since all occupied proton single-particle states contribute to it. Although these results were obtained for the Pb isotopes, they are general and applicable to any isotopic chain.

ACKNOWLEDGMENT

[1] I. Angeli and K. P. Marinova, At. Data Nucl. Data Tables **99**, 69 (2013).

[2] P. Campbell, I. Moore, and M. Pearson, Prog. Part. Nucl. Phys. **86**, 127 (2016).

[3] U. C. Perera, A. V. Afanasjev, and P. Ring, Phys. Rev. C **104**, 064313 (2021).

[4] S. E. Agbemava, A. V. Afanasjev, D. Ray, and P. Ring, Phys. Rev. C **89**, 054320 (2014).

[5] R. F. Garcia-Ruiz, M. L. Bissell, K. Blaum, A. Schwenk, J. Simonis, K. A. Wendt, and D. T. Yordanov, Nat. Phys. **12**, 594 (2016).

[6] A. Koszorús, X. F. Yang, W. G. Jiang, S. J. Novario, S. W. Bai, J. Billowes, C. L. Binnersley, M. L. Bissell, T. E. Cocolios, B. S. Cooper, R. P. de Groote, A. Ekström, K. T. Flanagan, C. Forssén, S. Franchoo, R. F. Garcia-Ruiz, F. P. Gustafsson, G. Hagen, G. R. Jansen, A. Kanellakopoulos *et al.*, Nat. Phys. **17**, 539 (2021).

[7] N. Tajima, P. Bonche, H. Flocard, P.-H. Heenen, and M. S. Weiss, Nucl. Phys. A **551**, 434 (1993).

[8] P.-G. Reinhard and H. Flocard, Nucl. Phys. A **584**, 467 (1995).

[9] C. Gorges, L. V. Rodríguez, D. L. Balabanski, M. L. Bissell, K. Blaum, B. Cheal, R. F. Garcia Ruiz, G. Georgiev, W. Gins, H. Heylen, A. Kanellakopoulos, S. Kaufmann, M. Kowalska, V. Lagaki, S. Lechner, B. Maaß, S. Malbrunot-Ettenauer, W. Nazarewicz, R. Neugart, G. Neyens *et al.*, Phys. Rev. Lett. **122**, 192502 (2019).

[10] T. Naito, T. Oishi, H. Sagawa, and Z. Wang, Phys. Rev. C **107**, 054307 (2023).

[11] S. A. Fayans, S. V. Tolokonnikov, E. L. Trykov, and D. Zawischa, Phys. Lett. B **338**, 1 (1994).

[12] S. A. Fayans, S. V. Tolokonnikov, E. L. Trykov, and D. Zawischa, Nucl. Phys. A **676**, 49 (2000).

[13] P.-G. Reinhard and W. Nazarewicz, Phys. Rev. C **95**, 064328 (2017).

[14] R. Rodríguez-Guzmán, P. Sarriguren, L. M. Robledo, and S. Perez-Martin, Phys. Lett. B **691**, 202 (2010).

[15] H. Nakada, Phys. Rev. C **92**, 044307 (2015).

[16] H. Nakada and T. Inakura, Phys. Rev. C **91**, 021302(R) (2015).

[17] H. Nakada, Phys. Rev. C **100**, 044310 (2019).

[18] M. M. Sharma, G. A. Lalazissis, and P. Ring, Phys. Lett. B **317**, 9 (1993).

[19] M. M. Sharma, G. Lalazissis, J. König, and P. Ring, Phys. Rev. Lett. **74**, 3744 (1995).

[20] T. Day Goodacre, A. V. Afanasjev, A. E. Barzakh, B. A. Marsh, S. Sels, P. Ring, H. Nakada, A. N. Andreyev, P. V. Duppen, N. A. Althubiti, B. Andel, D. Atanasov, J. Billowes, K. Blaum, T. E. Cocolios, J. G. Cubiss, G. J. Farooq-Smith, D. V. Fedorov, V. N. Fedosseev, K. T. Flanagan *et al.*, Phys. Rev. Lett. **126**, 032502 (2021).

[21] P. M. Goddard, P. D. Stevenson, and A. Rios, Phys. Rev. Lett. **110**, 032503 (2013).

[22] D. Vretenar, A. V. Afanasjev, G. A. Lalazissis, and P. Ring, Phys. Rep. **409**, 101 (2005).

[23] A. V. Afanasjev and S. Frauendorf, Phys. Rev. C **71**, 024308 (2005).

[24] G. A. Lalazissis, S. Karatzikos, R. Fossion, D. P. Arteaga, A. V. Afanasjev, and P. Ring, Phys. Lett. B **671**, 36 (2009).

[25] U. C. Perera and A. V. Afanasjev, Phys. Rev. C **106**, 024321 (2022).

[26] W. Bertozzi, J. Friar, J. Heisenberg, and J. W. Negele, Phys. Lett. B **41**, 408 (1972).

[27] M. Nishimura and D. W. L. Sprung, Prog. Theor. Phys. **77**, 781 (1987).

[28] C. J. Horowitz and J. Piekarewicz, Phys. Rev. C **86**, 045503 (2012).

[29] H. Kurasawa and T. Suzuki, Prog. Theor. Exp. Phys. **2019**, 113D01 (2019).

[30] P.-G. Reinhard and W. Nazarewicz, Phys. Rev. C **103**, 054310 (2021).

[31] T. Day Goodacre, A. V. Afanasjev, A. E. Barzakh, L. Nies, B. A. Marsh, S. Sels, U. C. Perera, P. Ring, F. Wienholtz, A. N. Andreyev, P. Van Duppen, N. A. Althubiti, B. Andel, D.

Atanasov, R. S. Augusto, J. Billowes, K. Blaum, T. E. Cocolios, J. G. Cubiss, G. J. Farooq-Smith *et al.*, Phys. Rev. C **104**, 054322 (2021).

[32] S. G. Nilsson and I. Ragnarsson, *Shapes and Shells in Nuclear Structure* (Cambridge University Press, Cambridge, 1995).

[33] J. Dobaczewski, W. Nazarewicz, J. Skalski, and T. Werner, Phys. Rev. Lett. **60**, 2254 (1988).

[34] M. Stoitsov, R. B. Cakirli, R. F. Casten, W. Nazarewicz, and W. Satuła, Phys. Rev. Lett. **98**, 132502 (2007).

[35] L. Bonneau, P. Quentin, and P. Möller, Phys. Rev. C **76**, 024320 (2007).

[36] G. Coló, H. Sagawa, and P. F. Bortignon, Phys. Rev. C **82**, 064307 (2010).

[37] A. V. Afanasjev and S. Shawaqfeh, Phys. Lett. B **706**, 177 (2011).

[38] J. Dobaczewski, A. V. Afanasjev, M. Bender, L. M. Robledo, and Y. Shi, Nucl. Phys. A **944**, 388 (2015).

[39] A. V. Afanasjev and E. Litvinova, Phys. Rev. C **92**, 044317 (2015).

[40] G. Hagen, M. Hjorth-Jensen, G. R. Jansen, R. Machleidt, and T. Papenbrock, Phys. Rev. Lett. **108**, 242501 (2012).

[41] G. R. Jansen, M. D. Schuster, A. Signoracci, G. Hagen, and P. Navrátil, Phys. Rev. C **94**, 011301(R) (2016).

[42] G. R. Jansen, J. Engel, G. Hagen, P. Navratil, and A. Signoracci, Phys. Rev. Lett. **113**, 142502 (2014).

[43] S. K. Bogner, H. Hergert, J. D. Holt, A. Schwenk, S. Binder, A. Calci, J. Langhammer, and R. Roth, Phys. Rev. Lett. **113**, 142501 (2014).

[44] E. Caurier, K. Langanke, G. Martínez-Pinedo, F. Nowacki, and P. Vogel, Phys. Lett. B **522**, 240 (2001).

[45] M. Bhuyan, B. Maheshwari, H. A. Kassim, N. Yusof, S. K. Patra, B. V. Carlson, and P. D. Stevenson, J. Phys. G **48**, 075105 (2021).

[46] P. Navrátil, S. Quaglioni, I. Stetcu, and B. R. Barrett, J. Phys. G **36**, 083101 (2009).

[47] B. R. Barrett, P. Navrátil, and J. P. Vary, Prog. Part. Nucl. Phys. **69**, 131 (2013).

[48] B. Nerlo-Pomorska and K. Pomorski, Z. Phys. A **344**, 359 (1993).

[49] Z. Lojewski, B. Nerlo-Pomorska, K. Pomorski, and J. Dudek, Phys. Rev. C **51**, 601 (1995).

[50] P. Federman and S. Pittel, Phys. Rev. C **20**, 820 (1979).